Final Draft

of the original manuscript

Yang, H.; Zander, D.; Jiang, B.; Huang, Y.; Gavras, S.; Kainer, K.; Dieringa, H.:

Effects of heat treatment on the microstructural evolution and creep resistance of Elektron21 alloy and its nanocomposite.

Effects of heat treatment on the microstructural evolution and creep resistance of Elektron21 alloy and its nanocomposite

Hong Yang [a]*, Daniela Zander [b], Bin Jiang [c, d]*, Yuanding Huang [a], Sarkis Gavras [a], Karl Ulrich Kainer [a], Hajo Dieringa [a]

[a] MagIC—Magnesium Innovation Center, Helmholtz-Zentrum Geesthacht, Max-Planck Straße 1, 21502, Geesthacht, Germany

[b] Chair of Corrosion and Corrosion Protection, Foundry Institute, RWTH Aachen University, Intzestr. 5, 52074, Aachen, Germany

[c] State Key Laboratory of Mechanical Transmissions, College of Materials Science and Engineering, Chongqing University, Chongqing 400044, China

[d] Chongqing Academy of Science and Technology, Chongqing 401123, China

* Corresponding author:

Hong Yang (hong.yang@hzg.de), Bin Jiang (jiangbinrong@cqu.edu.cn)

Abstract

In previously published research, creep resistance of commercial alloy Elektron21 (El21) and El21+1% AlN/Al nanocomposite were predominantly investigated in as-cast condition, little work focused on creep resistance following heat treatment. In this work, El21 and its nanocomposite with and without T6 treatment (520 °C for 8 h and 200 °C for 16 h) were prepared to reveal the influence of heat treatment on their microstructural evolutions and creep properties. Different intermetallic particles and precipitates that formed in El21 and El21+1% AlN/Al with different states were characterized using optical microscopy (OM), X-ray diffraction (XRD), scanning electron microscope (SEM) and transmission electron microscopy (TEM). Creep tests were performed over a stress range of 80-140 MPa at 240 °C. Creep results showed that the application of T6 treatment could improve the creep resistance of El21, but deteriorate that of El21+1% AlN/Al. This is attributed to the reduced amount of γ'' and β' precipitates in El21+1% AlN/Al (T6) after ageing, resulting from the formation of plate-like $Al_2(Nd, Gd)$ (Al_2RE) precipitates. It is also found that after T6 heat treatment, El21 (T6) had a lower minimum creep rate with a shorter duration of secondary creep stage than El21+1% AlN/Al (T6) at high creep temperatures due to the overageing of precipitates and the thermal stability of the Al_2RE particles. El21+1% AlN/Al nanocomposites, either in the as-cast or T6 condition, show a much longer duration of secondary creep than NP-free El21. The responsible

1   mechanism was attributed to the addition of AlN NPs and the formation of particulate/plate

2   Al_2RE phase.

3   Key words: magnesium alloys, Elektron21, nanocomposites, creep, heat treatment

1. Introduction

5   Creep is described as the slow plastic deformation over time under a constant applied stress

6   and elevated temperatures (above 0.4 T_m (absolute melting temperature)) [1]. The minimum

7   creep rate ($\dot{\varepsilon}_{min}$) is often regarded as a standard to evaluate the creep resistance of metallic

8   materials, which is identified as the minimum of the first derivative of the creep curves. The

9   dependence of $\dot{\varepsilon}_{min}$ on the applied stress σ and the temperature (in Kelvin) can be described

10   by the Norton-Arrhenius equation in Eq. (1) [2]:

11
$$\dot{\varepsilon}_{min} = A\sigma^n \ exp\left(-\frac{Q_c}{RT}\right) \tag{1}$$

12   Where A is the constant associated with the material, Q_c is the activation energy and R is the

13   gas constant (8.314 J/mol· K). n is the stress exponent which is commonly used to determine

14   the creep mechanisms.

15   It is well known that the major shortcoming in limiting the extensive use of magnesium (Mg)

16   alloys is their poor creep resistance at elevated temperatures. Especially for automotive power

17   train components, which often undergo a long-term exposure at high temperatures above

18   200 °C and stresses [3]. In order to address this problem, many heat resistant Mg-based alloys

19   have been developed over the past few decades, including Mg-Al-Ca (AX series) [4], Mg-Al-

20   Sr (AJ series) [5], Mg-Al-Ba-Ca [6, 7] and Mg-Al-Ca-Sr (MRI series) [8], Mg-Al-RE (AE

21   series) [9] and Mg-RE (rare earth) based alloys [10-14].

22   Magnesium Elektron Ltd (MEL) of Manchester, UK has produced an Mg-2.85Nd-0.92Gd-

23   0.41Zr-0.29Zn (wt.%) alloy named Elektron21 (El21) to provide excellent mechanical and

24   creep properties at elevated temperatures. It was designed to be an alternative alloy for WE43

25   (Mg-4Y-3RE-0.5Zr) from a cost-efficiency view [15]. Although El21 already has superior

26   creep properties at elevated temperatures, it was reported that there was still potential for

27   further improvement to its creep resistance. Katsarou *et al.* [16] found that with the addition of

28   AlN nanoparticles (NPs) and standalone Al NPs (AlN/Al) into El21 ultrasonically stirred, creep

29   resistance was significantly improved. However, the essential strengthening mechanism caused

by the addition of AlN/Al NPs was not discussed. Daudin *et al.* [17] further investigated AlN/Al NPs reinforced El21 to determine the fundamental role of NPs on microstructural modification. Daudin *et al.* [15] proposed that AlN/Al NPs has an indirect role in modifying the dendritic microstructure of intermetallic particles. These NPs partially reacted with Zr present in El21. Unfortunately, a detailed description on the interactions between AlN/Al NPs and alloying elements in El21 was still absent.

Saboori *et al.* [18] observed many discernible AlN clusters in El21+1 wt.% AlN/Al nanocomposites, suggesting that ultrasound-assisted stirring was insufficient to distribute the NPs homogeneously. In previous work [19] a novel stirring method called high shearing dispersion technique (HSDT) was applied to disperse the AlN/Al NPs in El21. It shows that the agglomeration of NPs in El21 was obviously alleviated with the assistance of HSDT. Compared to nanocomposites prepared by the traditional ultrasound-assisted stirring, a significant improvement to creep resistance of El21+0.5 wt.% AlN/Al nanocomposites was achieved [19, 20]. Moreover, the individual and synergistic effects of pure Al and AlN NPs on microstructural evolution and creep resistance of as-cast El21 were systematically investigated [21, 22]. It was revealed that the additions of Al or AlN both have positive effects on the creep resistance of El21 [21, 22]. With the simultaneous addition of Al and AlN NPs, a synergistic effect on the improvement of creep resistance in El21 was observed.

Both of the El21 and El21+AlN/Al nanocomposite are normally used in the as-cast condition [16, 19, 20, 22]. Few studies are focused on the heat treated El21 and its nanocomposites. Nd which is an alloying addition in El21 has a maximum solid solubility of 3.63 wt.% (0.63 at.%) in Mg at the eutectic temperature of 552 °C. The solubility decreases to approximately zero at 200 °C [23]. This phenomenon suggests that the addition of Nd in Mg could cause a potential precipitation hardening effect via heat treatment at a lower temperature [23] [24]. The Gd in El21 has a high solubility in Mg (23.48 wt.%, 4.53 at.%), which is much higher than Nd at the Mg-Gd eutectic temperature of 542 °C [24]. Smola *et al.* [25] reported that the addition of Gd in Mg resulted in better creep resistance especially after heat treatment. They found Mg-15Gd had the most noticeable strengthening effect after T6 treatment among their investigated alloys including WE43 and Mg-10Gd alloys. Kiełbus *et al.* [26] verified that El21 is a fully heat treatable alloy. It could exhibit optimum mechanical properties after T6 treatment (520 °C for 8 h and 200 °C for 16 h) [27]. Since El21 has a relatively high concentration of Nd and Gd, the microstructural evolution caused by the T6 treatment for the El21 and its nanocomposites needs

to be investigated in order to understand the effects of T6 heat treatment on the creep properties of El21 and El21+AlN/Al nanocomposites.

In this work, El21 and El21+AlN/Al nanocomposites were fabricated using HSDT followed by T6 heat treatment. Both the as-cast El21 and El21+AlN/Al nanocomposites were prepared following the same casting procedure for comparison. The influence of T6 heat treatment on the microstructural evolutions of El21 and its nanocomposites were investigated. The response of El21 and its nanocomposite to heat treatment on creep properties were characterized. Their responsible mechanisms for creep deformation were also discussed in association with their microstructural evolution.

2. Experimental procedures

The commercially available alloy El21 was selected as the base material to fabricate the nanocomposites. Its chemical composition was determined using optical emission spectroscopy (OES) and X-ray fluorescence (XRF) analysis to be Mg-2.85Nd-0.92Gd-0.41Zr-0.29Zn (all compositions are given in wt. % unless specified). A mixture of AlN and Al (hereafter, shorted as AlN/Al) NPs, which contains 75 % AlN and 25 % Al [16], was selected as the reinforcement to manufacture the El21-based nanocomposites. These NPs were produced using electrical explosion of Al wires under the atmosphere of argon (Ar) and nitrogen (N_2) at Tomsk State University (Russia) [28]. El21 with a weight of approximately 12 kg was melted at 720 °C in a mild steel crucible under the protective atmosphere of Ar and 1 % SF_6. 1 % AlN/Al NPs were added into the melt using a HSDT at 3000 rpm for 1 min. Such high shearing is utilized to distribute the AlN/Al NPs uniformly into the El21 melt. The device used to produce the HSDT is comprised of a stator and a rotor. It has a maximum shearing speed of 3000 rpm. The detailed description of HSDT and its principle can be found in [19, 29-32]. After intensive shearing, the melt was poured into a cylindrical mould preheated to 450 °C and then delivered to a three-zone furnace at 670 °C for 5 min. After this, the mould was lowered into a room temperature water bath for quenching at a descending speed of 100 mm/min. T6 heat treatment was performed for both the El21 and El21+1% AlN/Al nanocomposites. The solution treatment was performed at 520 °C for 8 h followed by quenching in hot water (60-80 °C) (T4) and then ageing at 200 °C for 16 h prior to air cooling. This T6 treatment has been investigated and confirmed by Kiełbus *et al.* [26] to produce a peak-hardening effect in El21. Luxfer MEL Technologies also recommended the same heat

4

1   treatment parameters to obtain the optimum mechanical properties in El21 [33]. The detailed

2   parameters for the investigated alloys are shown in Table 1.

3   Table 1. Casting parameters of as-cast and T6-treated El21 and El21+1% AlN/Al

4   nanocomposite.

Condition	Material	Shearing speed [rpm]	Shearing time [min]
As-cast	El21	3000	1
	El21+1% AlN/Al	3000	1
T6	El21 (T6)	3000	1
	El21+1% AlN/Al (T6)	3000	1

5   The cylindrical creep samples were machined from ingots with a diameter of 6 mm and a height

6   of 15 mm. Compressive creep measurements were carried out under constant stresses of 80,

7   100, 120 and 140 MPa at 240 °C, respectively. The reasons for choosing 240 °C as the working

8   temperature are mainly due to the following three aspects. Firstly, to compare with previous

9   creep results of El21 and its nanocomposites, the creep temperature in the present work is

10   identical to that used in [21] (240 °C). Secondly, it was reported [34] that El21 was designed

11   to work at temperatures up to 200 °C with excellent mechanical properties. In some powertrain

12   applications, service temperature is above 200 °C, such as engine pistons up to 300 °C [35]. It

13   is therefore of interest to understand the creep behavior of El21 and its nanocomposites when

14   the temperature is above 200 °C, such as at 240 °C. Lastly, since El21 already has excellent

15   creep properties at elevated temperatures, the secondary creep duration in tests at lower

16   temperatures would be exceedingly long and thus are avoided. The creep strains were recorded

17   with respect to creep time using an extensometer. Creep experiments were interrupted when

18   the minimum creep rates of these materials were achieved. If the tertiary creep stages of these

19   materials did not occur after a relatively long period of creep testing, their minimum creep rate

20   could not be identified. In this case, their final creep rates in the secondary creep stage were

21   considered as the minimum creep rates.

22   The specimens for microstructural observations were cold mounted with plastic resin, ground

23   using silicon carbide emery papers (500-2500 grit) and polished with OPS (diamond

24   suspension and colloidal silica) [36]. To reveal the optical microstructures (OM), the samples

25   were etched by an acetic/picric acid etchant [37], and investigated with a Leica DMI5000

26   microscope with a digital camera. Average grain size was measured using the linear intercept

27   method [38] by drawing positioned line segments on the OMs. The ratio of line length to

28   intercept number were considered as the average grain size. At least 3 OM micrographs or 200

29   grains were used to calculate the average grain size. Back scattered electron (BSE) observations

were carried out on a scanning electron microscope (SEM, Tescan Vega3, Czech Republic) with a Tescan energy dispersive X-ray spectrometer (EDS, IXRF Systems 550i, USA). Area fraction of the intermetallic particles was calculated quantitatively using ImageJ software [39] on at least 3 BSE micrographs. X-ray diffraction (XRD) patterns were characterized using a diffractometer with Cu radiation (wave length λ= 0.15406 nm) at 40 kV and 40 mA (Siemens D5000). The samples for Transmission electron microscopy (TEM) were ground to approximately 60 μm and then prepared by twin-jet electropolishing at −45 °C and a voltage of 50 V. Philips CM 200 and FEI TECNAI G2 F20 TEMs operated in bright-field mode at 200 kV were used to further investigate the microstructures of the alloys. The selected area diffraction patterns (SADPs) were to acquire their corresponding diffraction patterns of regions of interest. The calculation and measurement on the d-spacing of the nearest diffraction spots and angle between their vectors could give the information of crystal structure [40]. The phase from the crystallographic database matches with this obtained crystal structure was then identified and considered as its existence in the investigated alloys. Further fundamental principles of SADPs and their identification methods can be found in [41, 42]. The phase diagram of Mg-0.92Gd-xNd (wt. %) was calculated using thermodynamic software Pandat (CompuTherm LLC, USA) with the database PanMg2017 [43].

3. Results

3.1 Microstructural investigations

3.1.1 Optical microstructures and phase identifications

Fig. 1 presents the optical microstructures of El21 and El21+1% AlN/Al in the as-cast and T6 conditions. For comparison, the microstructures of samples which were only subjected to solid solution heat treatment (T4) at 520 °C for 8 h without the subsequent ageing are shown (Fig. 1(b) and (e)). The average grain size of El21 (T4) is 48.1±1.7 μm (Fig. 1(b)). It has no significant change compared to that of as-cast El21 (59.4±1.6 μm). With further ageing treatment at 200 °C for 16 h (Fig. 1(c)), there is still no noticeable grain coarsening for El21 (T6) with an average grain size of 41.1±1.3 μm. In the as-cast El21, many intermetallic particles were formed along the grain boundaries (Fig. 1(a)). After T4 treatment at 520 °C for 8 h, these particles were mostly dissolved into the α-Mg matrix (Fig. 1(b)). A smaller amount of intermetallic particles were observed in both El21 (T4) and El21 (T6) alloys (red arrows in Fig. 1(b-c)). For El21+1% AlN/Al nanocomposite, no apparent grain coarsening was observed after T4 or T6 treatment (Fig. 1(d-f)). Similarly, a large amount of intermetallic particles was

1 dissolved into the matrix after T4 or T6 treatment (Fig. 1(e-f)). Interestingly, in both El21+1%

2 AlN/Al (T4) and El21+1% AlN/Al (T6), many plate-like parallel precipitates were newly

3 formed inside α-Mg grains (purple arrows in Fig. 1(e-f)). Such precipitates were not observed

4 in NP-free El21.
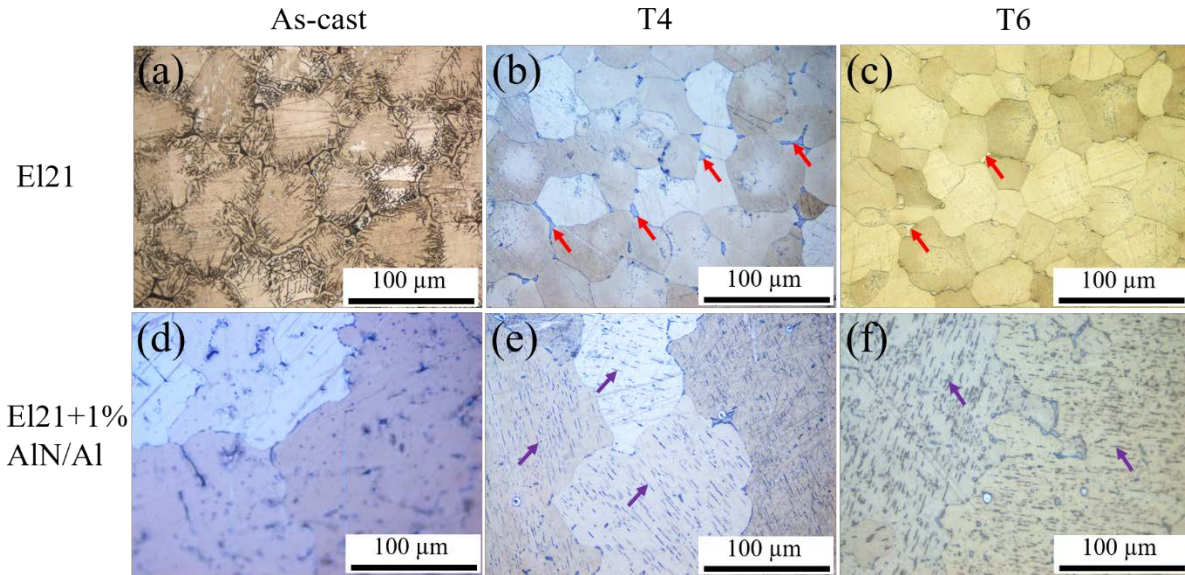
Fig. 1. Optical microstructures of (a) as-cast El21, (b) El21 (T4), (c) El21 (T6), (d) as-cast
El21+1% AlN/Al, (e) El21+1% AlN/Al (T4) and (F) El21+1% AlN/Al (T6), respectively.

8 Fig. 2 shows the XRD patterns of El21 and El21+1% AlN/Al in the as-cast, T4 and T6

9 conditions. The as-cast El21 is mainly composed of α-Mg and Mg_3(Nd, Gd) (Mg_3RE)

10 intermetallic particles (Fig. 2(a)). After T4 at 520 °C for 8 h, part of Mg_3RE intermetallic still

11 remains in El21 (T4) (Fig. 2(b)). The intensity of their corresponding diffraction peaks

12 noticeably decreases. After ageing treatment, the peaks of Mg_3RE disappeared for the El21

13 (T6). Instead, Mg_{41}(Nd, Gd)$_5$ ($Mg_{41}RE_5$) peaks were detected (Fig. 2(c)). The as-cast El21+1%

14 AlN/Al nanocomposite is predominantly composed of α-Mg, Mg_3RE and Al_2(Nd, Gd) (Al_2RE)

15 phases (Fig. 2(d)). However, these Mg_3RE peaks were difficult to be detected following T4

16 treatment. Only the Al_2RE phase remains stable in the El21+1% AlN/Al (T4) (Fig. 2(e)). After

17 ageing treatment, no additional phases were observed in the El21+1% AlN/Al (T6)
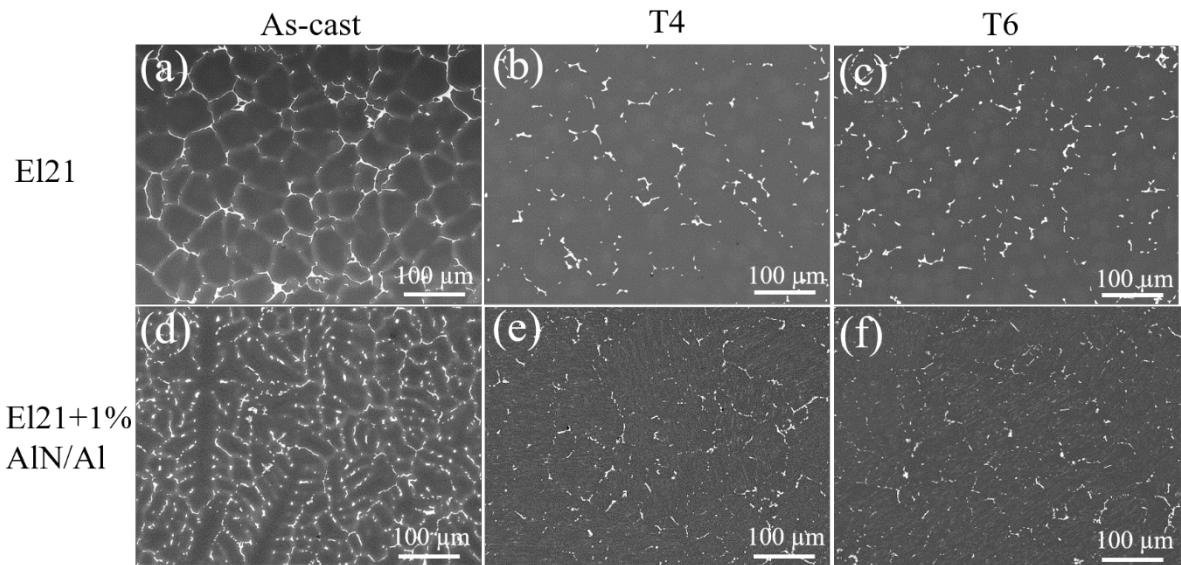
18 nanocomposite except for the Al_2RE phase (Fig. 2(f)).
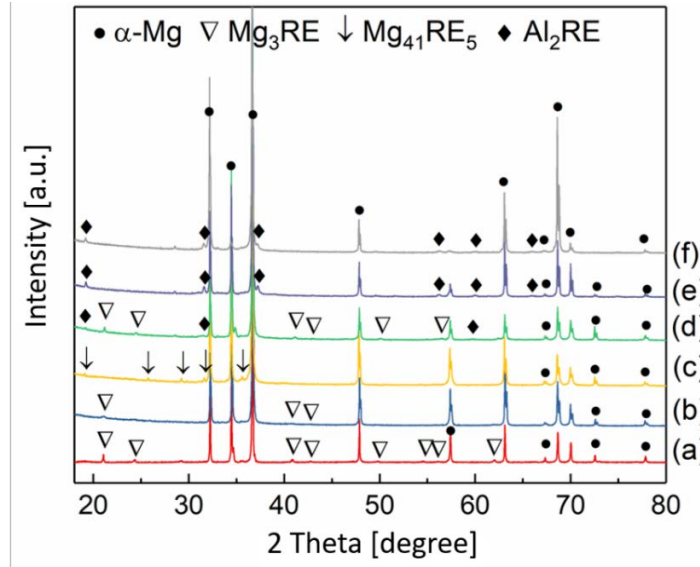
Fig. 2. XRD patterns of (a) as-cast El21, (b) El21 (T4), (c) El21 (T6), (d) as-cast El21+1% AlN/Al, (e) El21+1% AlN/Al (T4) and (f) El21+1% AlN/Al (T6).

3.1.2 Intermetallic characterizations

The intermetallic morphologies of El21 and El21+1% AlN/Al in the as-cast, T4 and T6 conditions are shown in Fig. 3. A summary of different intermetallic particles and precipitates formed in these materials is shown in Table 2. After T4, a relatively large amount of Mg_3RE phase was dissolved into the matrix of El21 (T4). The intermetallic area fraction decreased from 3.9 % in the as-cast El21 to 2.6 % in El21 (T4) (Fig. 3(a-b), Table 2). After the subsequent ageing treatment, no obvious changes in the area fraction of intermetallic particles as well as its morphology were observed (Fig. 3(c)). However, according to the XRD results, the dominant Mg-RE phase was transformed from Mg_3RE in El21 (T4) to $Mg_{41}RE_5$ in El21 (T6) (Fig. 2(b-c)). In as-cast El21+1% AlN/Al, Mg_3RE and Al_2RE are the two dominant phases, which have a higher area fraction (6.7 %) than as-cast El21 (Fig. 3(d)). After T4 treatment, the area fraction of intermetallic particles decreased from 6.7 % in as-cast El21+1% AlN/Al to 2.5 % in El21+1% AlN/Al (T4) (Fig. 3(e)). XRD results confirm that the remaining intermetallic particles in El21+1% AlN/Al (T4) are predominantly Al_2RE (Fig. 2(e)). It can then be concluded that the dissolved particles should be Mg_3RE phase during solution treatment. With the subsequent ageing treatment, these Al_2RE particles also remained stable in El21+1% AlN/Al (T6) (Fig. 3(f)).

| | As-cast | T4 | T6 |
| El21 | (a) 100 µm | (b) 100 µm | (c) 100 µm |
| El21+1% AlN/Al | (d) 100 µm | (e) 100 µm | (f) 100 µm |

Fig. 3. BSE micrographs of (a) as-cast El21, (b) El21 (T4), (c) El21 (T6), (d) as-cast El21+1% AlN/Al, (e) El21+1% AlN/Al (T4) and (f) El21+1% AlN/Al (T6), respectively.

Table 2. Summary of different intermetallic particles and precipitates formed in as-cast El21, El21 (T4), El21 (T6), as-cast El21+1% AlN/Al, El21+1% AlN/Al (T4) and El21+1% AlN/Al (T6).

| Materials | Intermetallic particles | | precipitates |
	Phase	Fraction	
El21	Mg_3RE	3.9 %	-
El21 (T4)	Mg_3RE	2.6 %	-
El21 (T6)	$Mg_{41}RE_5$	3.1 %	γ'' and β' (more)
El21+1% AlN/Al	Mg_3RE+Al_2RE	6.7 %	-
El21+1% AlN/Al (T4)	Particulate Al_2RE	2.5 %	-
El21+1% AlN/Al (T6)	Particulate Al_2RE	2.1 %	γ'' and β' (less)+plate Al_2RE

BSE micrographs at higher resolution are shown for further microstructural analysis (Fig. 4). Many short lath-like particles were formed adjacent to the Mg_3RE phase in the as-cast El21, which were assumed to be $Mg_{12}Nd$ phase due to the precipitation of supersaturated solid solution of Nd element [22]. After T4 or T6 treatment, these $Mg_{12}Nd$ particles dissolved into solid solution. During these heat treatments, no additional phases were formed in this alloy (Fig. 4(b-c)). In the El21+1% AlN/Al (T4) and El21+1% AlN/Al (T6) nanocomposites, a high-density of plate precipitates were observed in the α-Mg matrix after T4 or T6 treatments (green arrows in Fig. 4(e-f)). They are oriented parallel to each other and are relatively small size compared to the bright Al_2RE phase.

9
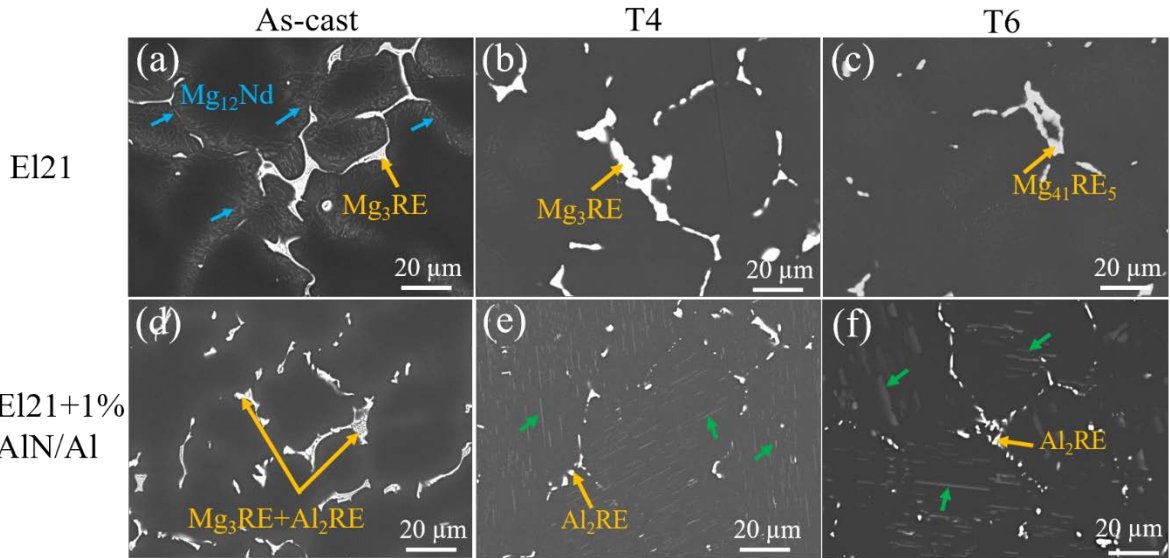
Fig. 4. BSE micrographs of (a) as-cast El21, (b) El21 (T4), (c) El21 (T6), (d) as-cast El21+1% AlN/Al, (e) El21+1% AlN/Al (T4) and (f) El21+1% AlN/Al (T6).

The EDS elemental maps in El21+1% AlN/Al (T6) are shown in Fig. 5. The intermetallic particles in Fig. 5(a) (orange arrows) are highly concentrated in Nd, Gd and Al (Fig. 5(c, d and h)). This result is in good agreement with the aforementioned XRD result that Al_2RE is the dominant phase in El21+1% AlN/Al (T6). Interestingly, as indicated by the white circles in Fig. 5, the particles with high concentrations of Nd and Gd elements and low concentrations of Al were detected. Higher magnification observations in combination with EDS analysis at such locations demonstrated that the particles marked with orange arrows have high concentrations of Mg and RE elements (Fig. 6(a-b)). This proves that some Mg-RE particles still remain in El21+1% AlN/Al (T6), although they could not be detected by XRD due to their low concentrations. In addition, at a higher magnification, the clusters of AlN NPs were also found in El21+1% AlN/Al (T6)), implying their greater thermal stability during melting and after heat treatments (Fig. 6(c-d)).
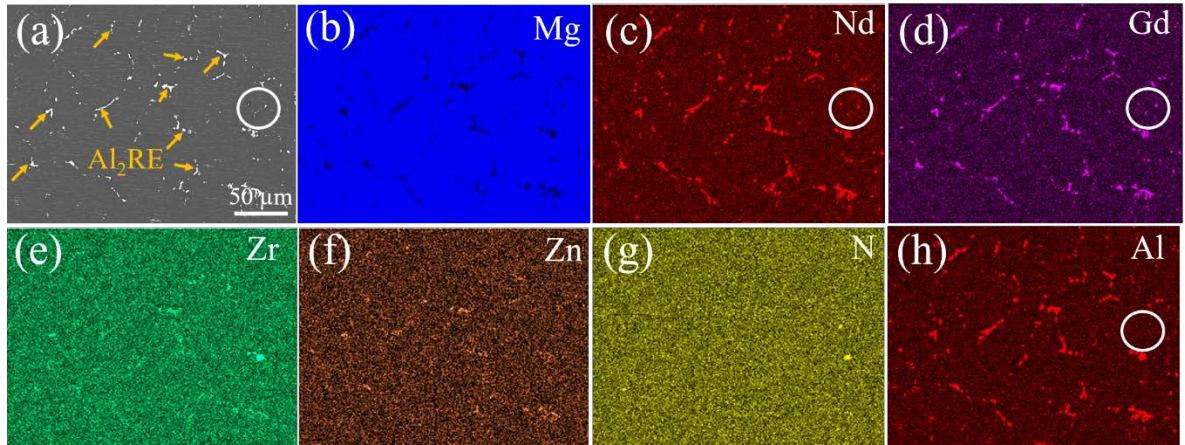
Fig. 5.(a) BSE micrograph and EDS mapping analyses of (b) Mg, (c) Nd, (d) Gd, (e) Zr, (f) Zn, (g) N and (h) Al in El21+1% AlN/Al (T6).
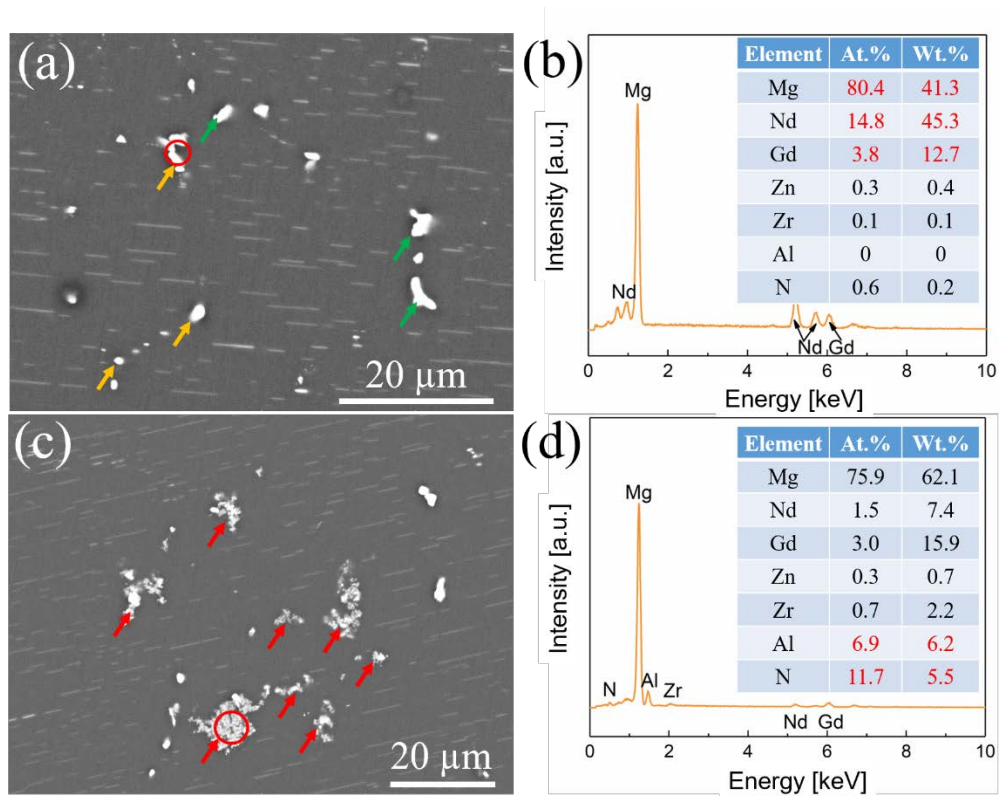
Fig. 6. (a) BSE micrographs of El21+1% AlN/Al (T6) showing the Mg-RE phase, (b) corresponding EDS point measurement of "red circle" position in (a), (c) BSE micrographs of El21+1% AlN/Al (T6) showing the AlN NPs and (d) corresponding EDS point detection of "red circle" position in (c).

1   3.1.3   TEM characterizations

2   The TEM bright-field micrograph in Fig. 7(a) shows the intermetallic morphology in El21 (T6).

3   Its corresponding diffraction pattern was obtained along $[11\bar{2}]_p$ zone axis (the subscript letter

4   "p" indicates the particle) (Fig. 7(b)). It can be indexed as $Mg_{41}RE_5$ phase with tetragonal

5   structure (a=1.47 nm, c=1.04 nm) [44]. This $Mg_{41}RE_5$ phase is the same as that detected by

6   XRD (Fig. 2(c)).
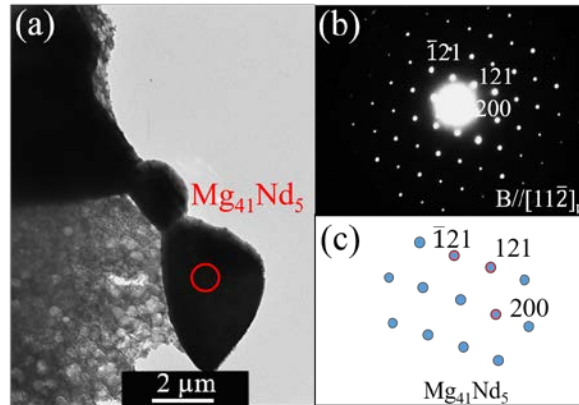
7

8   Fig. 7. TEM bright field micrograph of El21 (T6) and its corresponding SADP. (a) $Mg_{41}Nd_5$

9   and (b) SADP along $[11\bar{2}]_p$ zone axis and (c) schematic diagram of (b).

10   Fig. 8(a) shows the TEM bright field micrograph of Al_2RE phase in El21+1% AlN/Al (T6),

11   which is confirmed by the SADP along $[01\bar{1}]_p$ zone axis (Fig. 8(b-c)). Al_2RE phase has a

12   particulate shape with a face-centered cubic structure (a=0.80 nm [45]), which was also

13   observed previously [46]. The existence of particulate $Mg_{41}RE_5$ in El21+1% AlN/Al (T6) was

14   also confirmed with its corresponding SADP along $[2\bar{4}5]_p$ zone axis (Fig. 8(d-f)). The parallel

15   plate precipitates observed in El21+1% AlN/Al (T6) (Fig. 4(f)) were characterized along

16    $[\bar{1}2\bar{1}0]_m$ (the subscript letter "m" indicates Mg-matrix) and $[\bar{1}12]_p$ zone axis (Fig. 8(g-i)). This

17   plate-like Al_2RE phase has basal plane of Mg matrix as its habit plane.
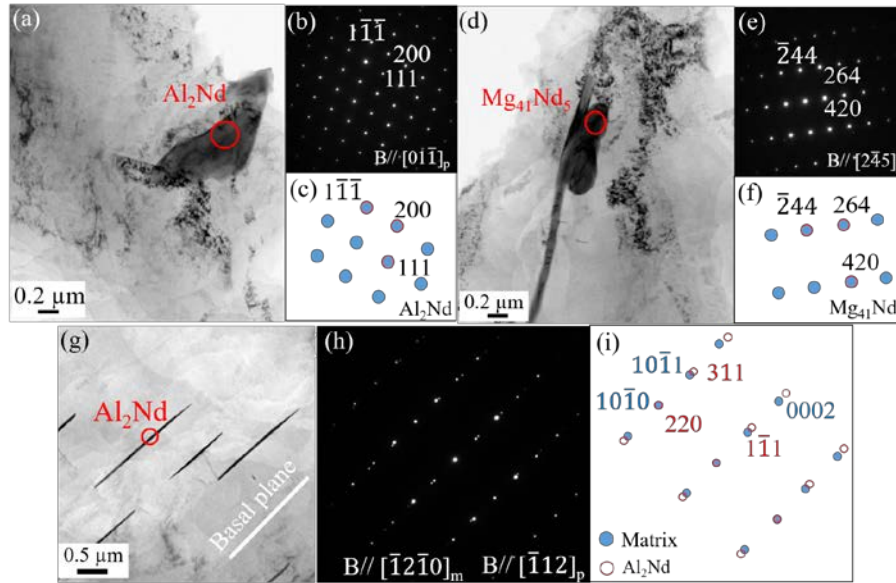
Fig. 8. TEM bright field micrographs of El21+1% AlN/Al (T6) and corresponding SADPs. (a-c) particulate Al_2RE phase along $[01\bar{1}]_p$ zone axis, the corresponding SADP and schematic diagram of (b), (d-f) $Mg_{41}Nd_5$ phase along $[2\bar{4}5]_p$ zone axis, the corresponding SADP and schematic diagram of (e) and (g-i) plate Al_2RE phase, the corresponding SADP and schematic diagram of (h). Two different diffraction patterns were identified along $[\bar{1}2\bar{1}0]_m$ and $[\bar{1}12]_p$ zone axis in (i).

As a result of T4 solution treatment, the RE present in the intermetallic went into solid solution. During the subsequent ageing treatment at 200 °C, RE solute precipitated as nano-sized particles. The TEM bright-field micrographs in Fig. 9(a) show two types of nano-sized precipitates in El21 (T6). The first having fine parallel plates which were observed by taking the incident beam parallel to the $[\bar{1}2\bar{1}0]_m$ of the matrix (orange arrows Fig. 9(a-c)). They are formed on the $(10\bar{1}0)$ prismatic planes perpendicular to the basal planes. According to Kiełbus *et al.* [47], these prismatic plates are likely β' phase, which was also observed in the ageing treated Mg-3Nd-Zr alloy [48]. The prismatic plane β' phase was reported to have an orthorhombic structure (a=0.64 nm, b=1.14 nm, c=0.52 nm) with a lenticular morphology. Its chemical composition is similar to that of Mg_7Nd [23]. The second precipitate type has nano-sized plate-like shape with their habit planes parallel to basal planes of Mg matrix (Fig. 9(d-f)). They are the γ'' phase, which was also found in a Mg-Nd-Zn alloy [49]. It is a basal plate phase with a hexagonal crystal structure (a=0.556 nm, c=0.521 nm), which is similar to that of $Mg_5(Ce,Zn)$.

13

In El21+1% AlN/Al (T6) nanocomposite, similar plate-like prismatic plane β' precipitates were also observed when the incident beam is parallel to the $[\bar{1}2\bar{1}0]_m$ (orange arrows, Fig. 9(h)). The basal plane γ" precipitates (green arrows) and β' prismatic precipitates (orange arrows) are perpendicular to each other as viewed using the incident beam parallel to the $[\bar{1}2\bar{1}0]_m$ (Fig. 9 (k)). It should be noted that a compositional difference exists between the prismatic plane precipitates in El21 (T6) and El21+1% AlN/Al (T6). The prismatic plane precipitates in El21+1% AlN/Al (T6) have a well-defined Al peak in EDS (Fig. 9 (n)), but no Al peak can be seen for prismatic plane precipitates in El21 (T6) (Fig. 9(g)).
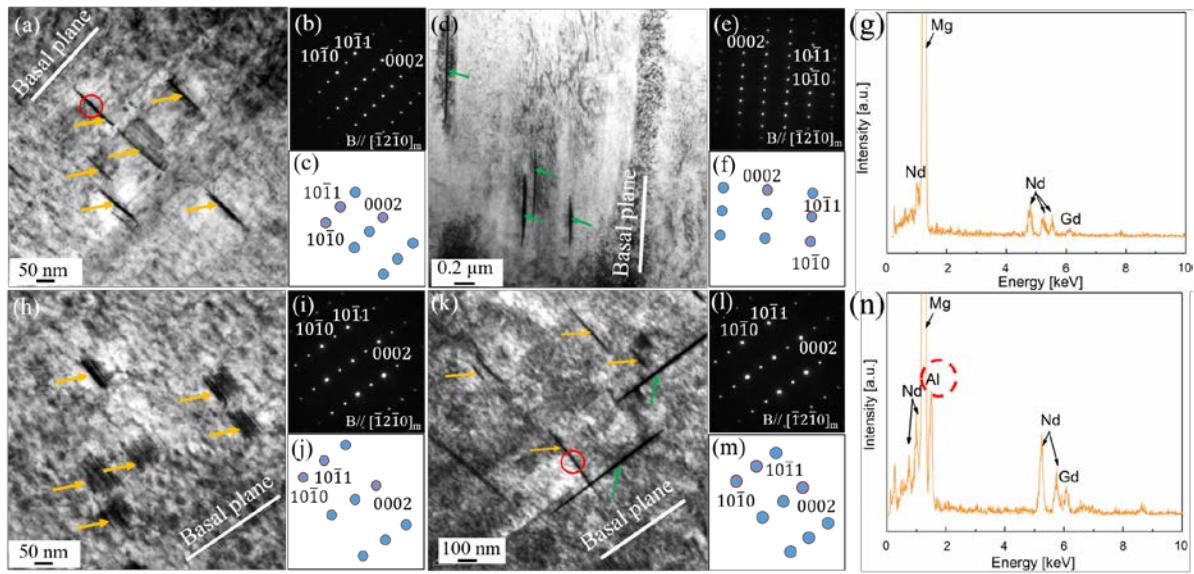
Fig. 9. (a-c) Prismatic plane β' precipitates along $[\bar{1}2\bar{1}0]_m$ in El21 (T6), its SADP and schematic diagram of (b), (d-f) basal plane γ" precipitates along $[\bar{1}2\bar{1}0]_m$ zone axis in El21 (T6), its SADP and schematic diagram of (e), (g) EDS result of the 'red circle' position in (a). (h-j) prismatic plane β' precipitates along $[\bar{1}2\bar{1}0]_m$ zone axis in El21+1% AlN/Al (T6), its SADP and schematic diagram of (i), (k-m) basal plane γ" and prismatic plane β' precipitates along $[\bar{1}2\bar{1}0]_m$ zone axis in El21+1% AlN/Al (T6), its SADP and schematic diagram of (l) and (n) EDS result of the 'red circle' position in (k).

Fig. 10 shows the microstructures of El21+1% AlN/Al (T6) after creep deformation from 120 MPa and at 240 °C. The micron scaled plate-like Al_2RE particles, which were originally parallel to each other inside the grains before creep testing (Fig. 4(f)), were curved after creep testing (Fig. 10(a-b)). In Fig. 10(c), the dislocations were effectively obstructed by β' precipitates in the crept El21+1% AlN/Al (T6), suggesting their greater strengthening effect during creep.
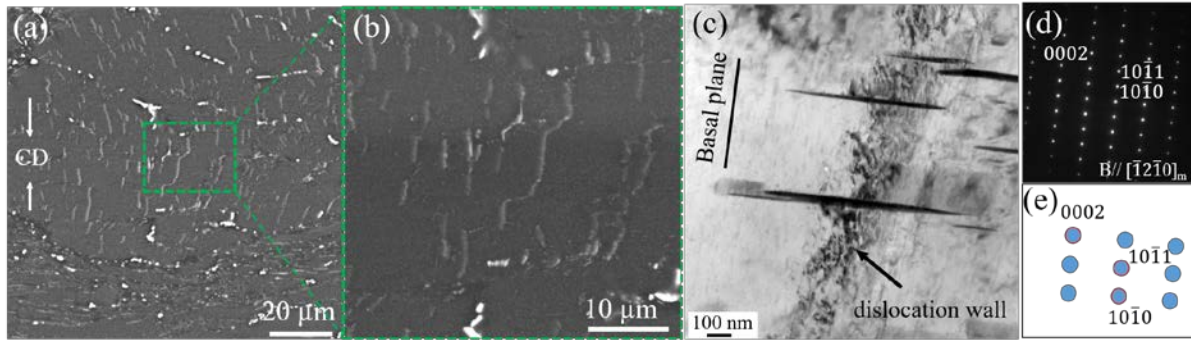
Fig. 10. (a-b) Lower and higher resolution BSE micrographs for El21+1% AlN/Al (T6) after creep tests at 240 °C under 120 MPa. The compressive direction (CD) is indicated with "white arrows" and (c-e) TEM bright field micrograph, its corresponding SADP and schematic diagram of SADP for El21+1% AlN/Al (T6) after creep tests at 240 °C under 120 MPa.

3.2 Creep behaviors

3.2.1 Creep properties

Fig. 11 shows the creep curves of strain over time for the as-cast El21, as-cast El21+1% AlN/Al, El21 (T6) and El21+1% AlN/Al (T6) under a stress range of 80-140 MPa at 240 °C, respectively. With an increase in the applied stress, the creep strains increase over time. The as-cast El21 exhibits the highest creep strain, indicating it has the worst creep resistance. After T6 treatment, the creep strain of El21 (T6) is lower than that of the as-cast El21, suggesting that T6 treatment can effectively improve its creep resistance. With the addition of 1% AlN/Al NPs in El21, the creep strains of as-cast El21+1% AlN/Al are obviously lower than that of as-cast El21 alloy. It indicates that 1% AlN/Al NPs could significantly improve the creep properties of as-cast El21 alloy, which was already reported in previous work [19]. However, unlike its positive strengthening effect on the creep resistance of monolithic El21, the execution of T6 treatment on El21+1% AlN/Al nanocomposites deteriorates its creep resistance instead.
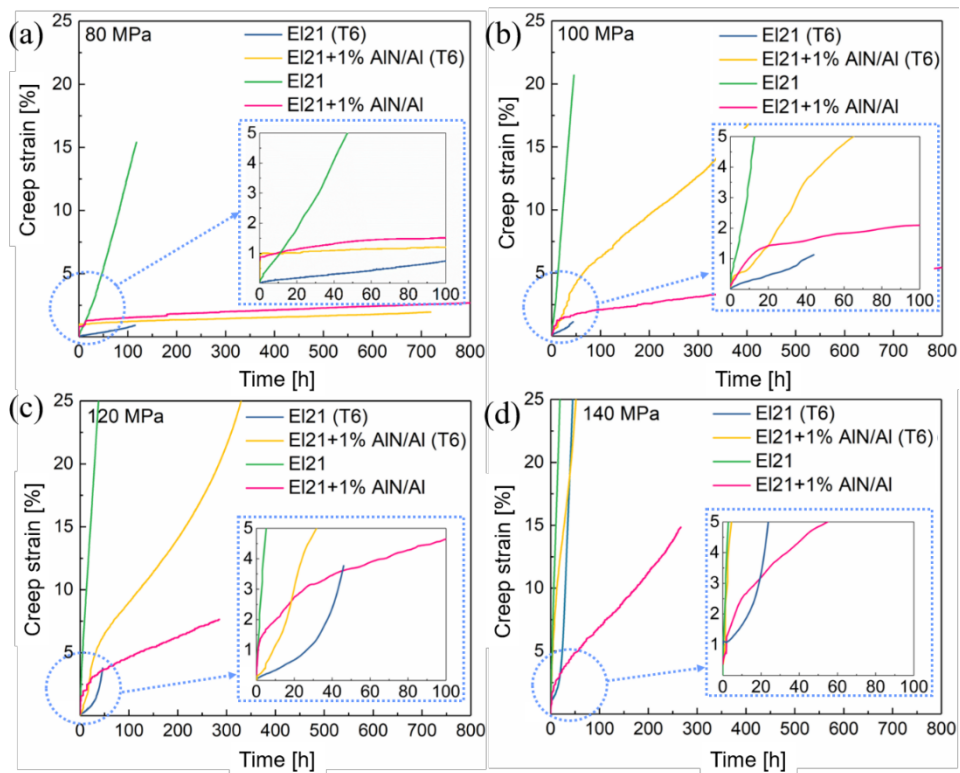
Fig. 11. Creep curves of strain over time for the as-cast El21 [21], as-cast El21+1% AlN/Al [21], El21 (T6) and El21+1% AlN/Al (T6) with applied stresses of (a) 80 MPa, (b) 100 MPa, (c) 120 MPa and (d) 140 MPa.

The curves of creep rate over time for the as-cast El21, as-cast El21+1% AlN/Al, El21 (T6) and El21+1% AlN/Al (T6) are shown in Fig. 12. In this work, the minimum creep rates were defined based on two situations. When the tertiary creep stage of the material in Fig. 12 has clearly begun, the minimum creep rate could be easily identified. When the tertiary creep stage does not occur after a relatively long creep duration, the final creep rate was regarded as the minimum creep rate. It is found that the minimum creep rate of El21 (T6) is distinctly lower than that of the as-cast El21 by approximately one order of magnitude under all the applied stresses (Table 3). After T6 treatment, with increases in the applied stresses, El21+1% AlN/Al (T6) shows a higher minimum creep rate than the as-cast El21+1% AlN/Al, suggesting that it has poorer creep properties than the latter.

Apart from their minimum creep rates in Fig. 12, the duration of the secondary creep stage is also noteworthy to describe the creep performance. As shown in Fig. 12, El21+1% AlN/Al nanocomposites always show a longer duration of secondary creep in either as-cast or T6 condition. Nevertheless, the NP-free El21 in either as-cast or T6 condition typically reach the tertiary creep stage faster (Fig. 12). For example, the tertiary creep stage of El21 (T6) occurred

16

rapidly after 93.2 h, 29.0 h, 13.9 h and 14.8 h under the stresses of 80, 100, 120 and 140 MPa, respectively (Fig. 12). In contrast, the as-cast El21+1% AlN/Al has no tertiary stage even following longer creep testing durations of 800 h, 800 h, 287.0 h and 266.8 h under the stresses of 80, 100, 120 and 140 MPa, respectively. In terms of engineering significance, it can be considered that the as-cast El21+1% AlN/Al and El21+1% AlN/Al (T6) have better creep resistance than the as-cast El21 and El21 (T6) alloys.
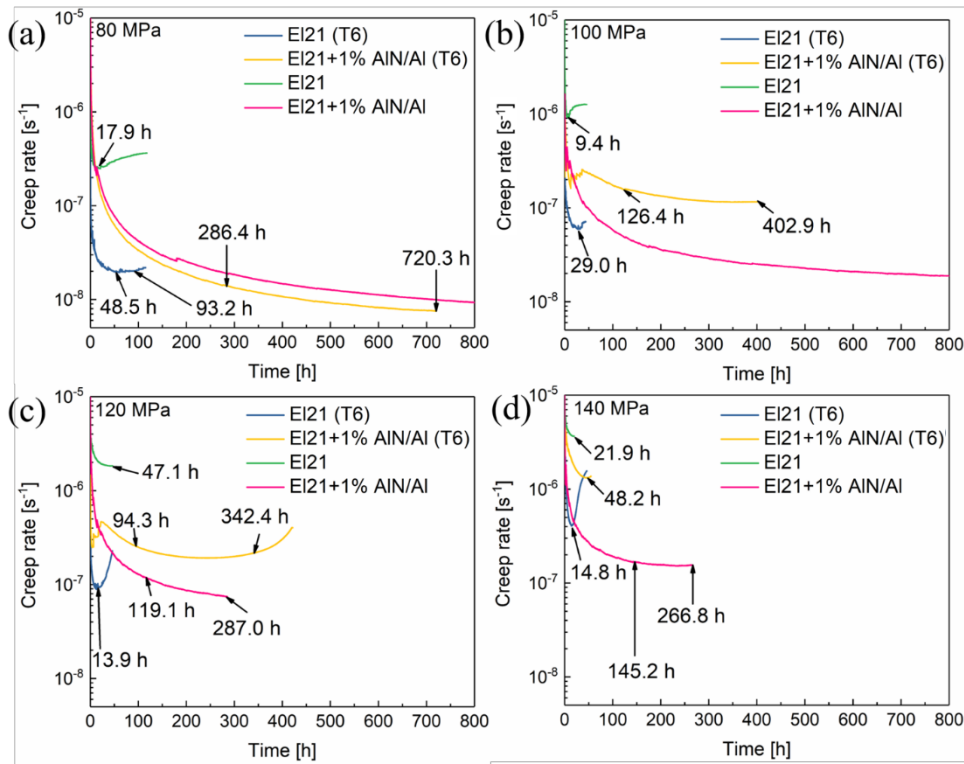
Fig. 12. Creep rates over time for the as-cast El21 [21], as-cast El21+1% AlN/Al [21], El21 (T6) and El21+1% AlN/Al (T6) under the stresses of (a) 80 MPa, (b) 100 MPa, (c) 120 MPa and (d) 140 MPa.

It is worth noting that El21 (T6) and El21+1% AlN/Al (T6) show inconsistent trends in the curves of creep rate over time. For example, El21 (T6) deformed more slowly in the primary stage of creep than El21+1% AlN/Al (T6) under 120 MPa (Fig. 11(c)). But after creeping for 13.9 h it deformed much more quickly (Fig. 12(c)). Its strain increases significantly and the tertiary creep stage occurs immediately. In contrast, although El21+1% AlN/Al (T6) deformed faster in the primary creep stage than El21 (T6) under 120 MPa (Fig. 11(c)), its strain rate becomes more stable and achieves a steady-state region during the creep time from 94.3 h-342.4 h (Fig. 12(c)).

Table 3. Minimum creep rates under the applied stresses of 80, 100, 120 and 140 MPa at 240 °C.

17

|	Stress [MPa]	El21 [21]	El21+1% AlN/Al [21]	El21(T6)	El21+1% AlN/Al (T6)
$\dot{\varepsilon}$ [s^{-1}]	80	2.5×10^{-7}	9.05×10^{-9}	1.96×10^{-8}	7.37×10^{-9}
	100	9.25×10^{-7}	1.87×10^{-8}	6.12×10^{-8}	1.15×10^{-7}
	120	1.83×10^{-6}	7.36×10^{-8}	9.16×10^{-8}	1.91×10^{-7}
	140	4.01×10^{-6}	1.52×10^{-7}	4.04×10^{-7}	1.33×10^{-6}

3.2.2 Creep mechanisms

The comparisons of minimum creep rates are shown in Fig. 13(a). Based on Eq. (1), the n values can be obtained by the slope of $\ln\dot{\varepsilon}_{min}$ against $\ln\sigma$ (Fig. 13(a)). The creep stress exponents are in a range of 4.9 - 8.7. El21+1% AlN/Al (T6) has the highest n value (8.7), which is too high to determine the creep mechanisms directly only according to such an n value. It is therefore necessary to introduce the threshold stress σ_{thr} to calculate the true stress exponent [50]. The interactions between particles/precipitates and dislocations are regarded as the origin of threshold stress [16]. Extrapolating Fig. 13(a) to a strain rate of 10^{-10} s^{-1} provides the threshold stress value for each alloy (Table 4). A detailed determination method can be found in [51]. With the introduction of σ_{thr}, Eq. (1) can then be described as follows:

$$\sigma_{eff} = \sigma - \sigma_{thr} \qquad (2)$$

$$\dot{\varepsilon}_{min} = A(\sigma_{eff})^{n_t} \exp\left(-\frac{Q_C}{RT}\right) \qquad (3)$$

The true stress exponent n_t values are then calculated by the slope of double logarithmic plots of $\ln\sigma_{eff}$ against $\ln\dot{\varepsilon}_{min}$. Their values are in a range of 3.4 - 4.6 (Fig. 13(b)). It is well known that $n=3$ is associated with the viscous glide of dislocation and $n=5$ is associated with the dislocation climb at elevated temperature [2, 11, 52]. Therefore, the present creep deformation mechanism for these four materials at 240 °C should be attributed to the viscous glide of dislocations and/or dislocation climb.
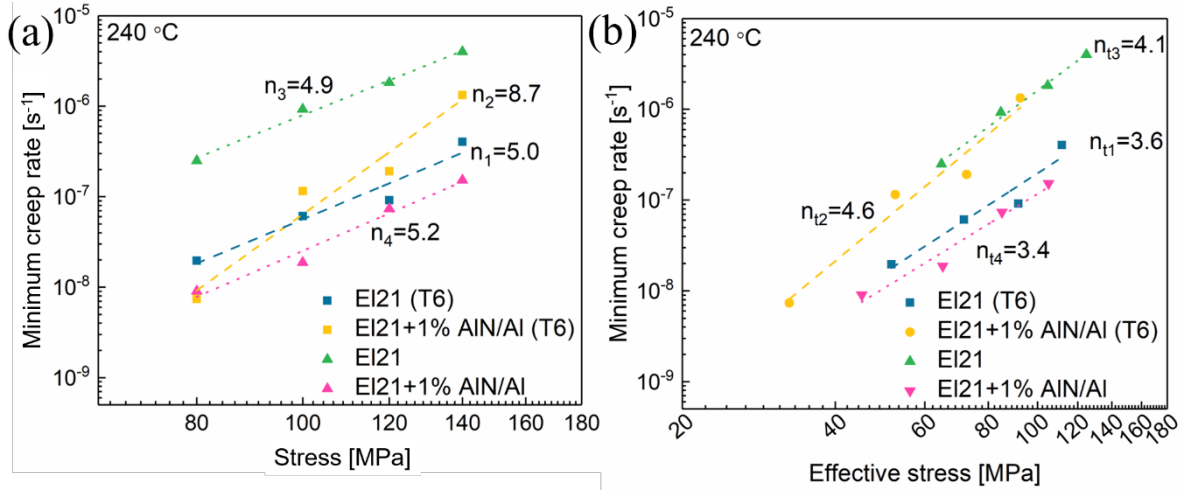
Fig. 13. Minimum creep rates against (a) applied stress and (b) effective stress for the as-cast El21 [21], as-cast El21+1% AlN/Al [21], El21 (T6) and El21+1% AlN/Al (T6).

Table 4. Stress exponents, threshold stresses and true stress exponents of the as-cast El21 [21], as-cast El21+1% AlN/Al [21], El21 (T6), El21+1% AlN/Al (T6).

| Materials	n	σ_{thr} [MPa]	n_t
El21	4.9	15.3	4.1
El21+1% AlN/Al	5.2	34.9	3.4
El21 (T6)	5.0	28.4	3.6
El21+1% AlN/Al (T6)	8.7	47.5	4.6

4 Discussion

4.1 Effect of heat treatment on the microstructure

4.1.1 Evolution of intermetallic particles

Fig. 14 shows the schematic diagrams of microstructural evolutions for El21 and El21+1% AlN/Al nanocomposites in the as-cast, T4 and T6 conditions, respectively. The as-cast El21 is made up of α-Mg matrix, a network of Mg$_3$RE intermetallic and short lath-like Mg$_{12}$Nd (Fig. 14(a)). Easton *et al.* [53] proposed that the Mg$_3$RE phase is a metastable phase with respect to Mg$_{41}$Nd$_5$ phase. Its formation occurs only at a relatively high cooling rate during solidification. In this work, the as-cast El21 was quenched by water with a descending speed of 100 mm/min. The cooling rate achieved by such quenching is enough to promote the formation of Mg$_3$RE during solidification. In addition, based on the Edge to Edge Matching (E2EM) model proposed by Zhang *et al.* [54-56], the crystallographic misfit of Mg$_3$RE phase with α-Mg phase is also

below 10 %, with the smallest below 0.5 %. This implies a favorable lattice match for Mg_3RE phase to nucleate and grow on the surface of α-Mg during solidification.

After T4 treatment, Mg_3RE particles with an area fraction of approximately 33 % were dissolved into the α-Mg matrix thus causing RE to go into solid solution (Fig. 14(b)). It was reported that Mg_3RE in El21 begins to dissolve into the matrix over a narrow temperature range from 528 to 534 °C [22]. The present solid solution temperature of 520 °C is quite close to the dissolution temperatures of Mg_3RE phase. Thus, after solid solution treatment for 8 h the Mg_3RE phase dissolved. Similarly, Nd element has enough time to diffuse homogeneously in the matrix and thus $Mg_{12}Nd$ dissolved in the matrix.
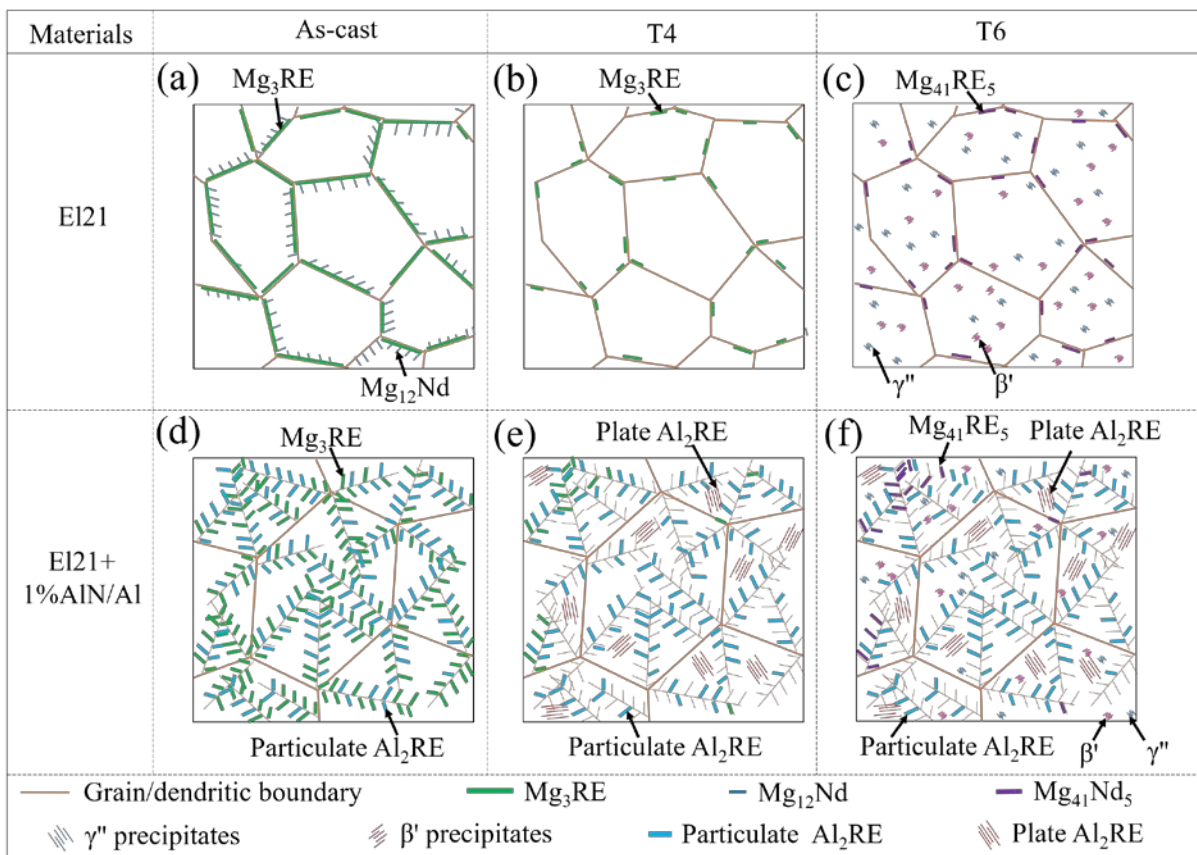

Fig. 14. Schematic diagrams of the microstructural evolutions for (a) as-cast El21, (b) El21 (T4), (c) El21 (T6), (d) as-cast El21+1% AlN/Al, (e) El21+1% AlN/Al (T4) and (f) El21+1% AlN/Al (T6).

Upon subsequent ageing treatment at 200 °C, the Mg_3RE particles along the grain boundaries were changed to $Mg_{41}Nd_5$ phase in El21 (Fig. 2(c) and Fig. 7(a)). The phase diagram of Mg-0.92Gd-xNd (wt.%) calculated using Pandat software is presented in Fig. 15. The phases for Mg-0.92Gd-2.85Nd (wt.%) includes α-Mg and $Mg_{41}Nd_5$ when the temperature is above

1   158.4 °C. It is therefore suggested that the $Mg_{41}Nd_5$ phase has enough time to be transformed

2   from Mg_3RE and to grow during ageing. Delfino *et al.* [57] also observed the peritectic reaction

3   of Mg_3Nd phase to $Mg_{41}Nd_5$ phase in Mg-Nd alloys.
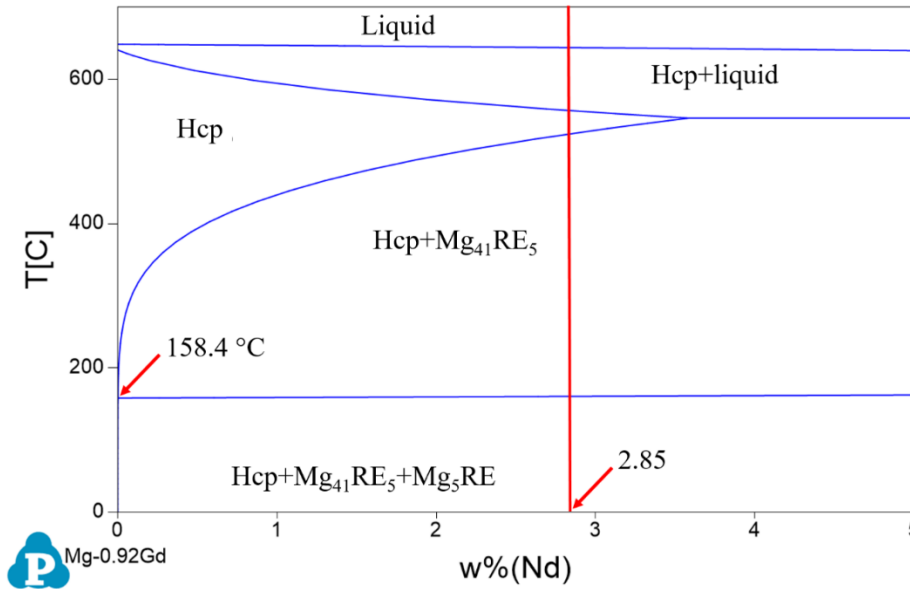
4

5   Fig. 15. Phase diagram of Mg-0.92Gd-xNd (wt. %) calculated using Pandat software with the

6   thermodynamic database PanMg2017.

7   4.1.2 Precipitate formation

8   After ageing treatment at 200 °C many nano-sized basal γ" precipitates and prismatic β'

9   precipitates were formed in El21 (T6) (Fig. 9(a-f)). The precipitation sequence in Zn-free Mg-

10   Nd alloy is normally as follows: supersaturation solid solution (SSSS) → G.P. (Guinier-Preston)

11   zone →β" → β' and $β_1$→ β in a temperature range of 60 to 350 °C [23, 58]. El21 is a Zn

12   containing Mg-Nd alloy. It was reported [48, 49, 59] that Mg-Nd-Zn alloy has a different

13   precipitation sequence: SSSS → G.P. zone → γ" → γ' → γ. Ma *et al.* [48] investigated the

14   effect of Zn on the precipitate formation in Mg-Nd alloys. They found that the addition of Zn

15   resulted in the formation of Nd-Zn rich phase lying on the basal planes. In this work, Nd and/or

16   Gd atoms were inclined to co-segregate with the Zn atoms to form many basal precipitates γ"

17   in El21 (T6). In El21 Zn has a relatively small content (0.29 %), which can only interact with

18   a certain amount of RE atoms to form the basal γ" precipitates. It can then be expected that the

19   rest of RE atoms in the Mg matrix precipitated following the same sequence that occurred in

20   Zn-free Mg-Nd alloy. Such a precipitation sequence leads to the formation of high density

21   prismatic β' precipitates in El21 (T6) (Fig. 9(a-c)).

In the as-cast El21+1% AlN/Al nanocomposite, Mg_3RE and Al_2RE are the two prominent intermetallic phases (Fig. 14(d)). Al_2RE has a significantly higher thermal stability with a melting point of 1200 °C and Mg_3RE phase has a melting point of 780 °C [60, 61]. Hence, Al_2RE phase does not dissolve into solid solution even after T4 treatment as opposed to most of Mg_3RE which does dissolve into solid solution (Fig. 14(e)).

It is worth noting that many micro-sized plate-like Al_2RE precipitates were newly formed in the center of the grains in El21+1% AlN/Al (T4) and El21+1% AlN/Al (T6) (Fig. 4(e-f)), which were not observed in NPs-free El21. The presence of plate-like Al_2RE precipitates is likely as a result of the addition of 1% AlN/Al NPs in El21. As reported in [62], based on the calculations of their Gibbs energies AlN could react with Zr to form ZrN and Al as follows: $Zr + AlN \rightarrow ZrN + Al$. Thus some of Al was additionally formed. When adding AlN/Al into El21, both AlN NPs and metallic Al could be regarded as the source of Al atoms to form Al_2RE precipitates. In the as-cast El21+1% AlN/Al nanocomposite, not all Al atoms reacted with RE to form particulate-shaped Al_2RE particles. Part of them did not have enough time to react with RE atoms due to the rapid cooling rate during solidification. According to the Mg-Al binary phase diagram [63], Al has a relatively high solid solubility with a maximum value of 12.9 wt. % in Mg at the eutectic temperature. The rest of the Al atoms which did not participate in the formation of particulate Al_2RE in the as-cast El21+1% AlN/Al nanocomposite can be dissolved into α-Mg matrix. During T4 treatment at the relatively high temperature of 520 °C, most of the Mg_3RE particles were dissolved and thus a large concentration of RE atoms go into solid solution. It was reported [64, 65] that Al is inclined to react with RE elements to form stable intermetallic particles, such as Al_2RE (face-centered cubic structure) and $Al_{11}RE_3$ (body-centered orthorhombic structure) in AE42 [66] and AE44 [67] alloys. Therefore, the solid solution of Al atoms in the α-Mg matrix could interact with the dissolved RE atoms to form the plate-like Al_2RE precipitates during T4 treatment. Previous investigations [22] verified that Al preferred to react with REs to form Al_2RE in α-Mg interiors rather than with Mg to form $Mg_{17}Al_{12}$ based on the calculation of their formation enthalpy. In El21+1% AlN/Al (T6) nanocomposite, similar nano-sized basal plane γ'' and prismatic plane β' precipitates were also observed (Fig. 9(h-m)). The reason that the prismatic plane β' precipitates have a high content of Al in this composite is also ascribed to the high affinity of Al to REs.

It is difficult to compare the amount of nano-sized precipitates in El21 (T6) and El21+1% AlN/Al (T6) intuitively owing to the limited observation areas with TEM. However, it can

1 reasonably be estimated that the amount of γ″ and β′ precipitates formed in El21+1% AlN/Al

2 (T6) is lower than that in El21 (T6). Since the total amount of RE atoms is equal. After T4

3 treatment, the additional formation of micro-sized plate-like Al_2Nd precipitates took a large

4 amount of RE atoms in the α-Mg matrix of El21+1% AlN/Al (T4), leading to the reduction in

5 the concentration of RE solid solution. Consequently, less RE atoms were available for the

6 formation of nano-sized precipitates during ageing treatment in El21+1% AlN/Al (T6)

7 nanocomposites than that in El21 (T6).

8 4.2 Effect of heat treatment on creep properties

9 Two strengthening mechanisms influence the creep resistance of El21 (T6), grain boundary

10 reinforcement and precipitation strengthening. After T6 treatment, the area fraction of

11 intermetallic particles was decreased from 3.9 % in the as-cast El21 to 3.1 % in El21 (T6)

12 (Table 2), indicating that less area fraction of grain boundaries were reinforced by intermetallic

13 particles. This in turn may lead to grain boundary sliding during creep and reduce the creep

14 resistance of El21 (T6). After T6 treatment El21 (T6) had many nano-sized γ″ and β′

15 precipitates in the matrix, which could act as barriers to effectively obstruct the dislocations

16 due to precipitate strengthening and improve creep resistance. Based on the present results, it

17 can be concluded that precipitation strengthening resulting from the nano-sized γ″ and β′ was

18 more effective in improving creep resistance than the decreased strengthening effect caused by

19 less grain boundary reinforcements. This is due to the Orowan strengthening where smaller

20 precipitates are usually more effective in hindering the dislocation movement than larger sized

21 ones [68].

22 Similarly, the creep resistance of El21+1% AlN/Al (T6) is also influenced by grain boundary

23 reinforcement and precipitation strengthening. However, unlike in El21 (T6), the improvement

24 of creep resistance originating from precipitation strengthening could not offset the reduction

25 of creep resistance caused by the lower amount of grain boundary reinforcement. Firstly, after

26 T6 treatment, approximately 68.7 % area fraction of intermetallic particles were dissolved into

27 the α-Mg matrix in El21+1% AlN/Al (T6), while only approximately 20.5 % area fraction of

28 intermetallic particles decreased in El21 (T6) (Table 2). The reduced area fraction of the

29 intermetallic particles in El21+1% AlN/Al (T6) is much higher than that in El21 (T6),

30 indicating the reduction of grain boundary reinforcement is much more in the former than that

31 in the latter. Lastly, as shown in Fig. 10(c), nano-sized β′ precipitates could effectively hinder

32 the dislocations during creep, which caused precipitation strengthening in E21+1% AlN/Al

(T6). However, the precipitation strengthening might be weakened in E21+1% AlN/Al (T6) due to the lower amounts of γ'' and β' precipitates than that in El21 (T6). Instead, many micro-sized Al_2Nd precipitates with plate morphology were additionally formed. They were observed to be curved under the compressive stresses (Fig. 10(a)), which were less effective in hindering dislocation motion. Hence, due to the simultaneously decreased grain boundary reinforcements and precipitation strengthening, the creep resistance of E21+1% AlN/Al (T6) was worse than that of as-cast E21+1% AlN/Al.

El21 (T6) has a lower minimum creep rate but a shorter duration of secondary creep than El21+1% AlN/Al (T6). Since El21 (T6) has a quite narrow secondary creep region, its minimum creep rate and the rates before the minimum creep rate reflect the process of primary creep. Therefore, the following two aspects are taken into account for the description of its creep behaviors. One is the primary stage of creep, which reflects the effect of work hardening at the initial deformation stage. The other is the duration of the secondary creep stage, which indicates the dynamic equilibrium between work hardening and thermal softening.

I.   Primary stage

It is known that the decrease of creep rate in the primary stage was attributed to the strain hardening or the decrease in the number density of free or mobile dislocations [69]. The degree of work hardening depends on the interactions between second phase/precipitates and dislocation movement. Since the area fraction of intermetallic particles in El21 (T6) and El21+1% AlN/Al (T6) are similar (Table 2), the nano-sized γ'' and β' precipitates play a more important role in causing work hardening during deformation in the primary creep stage. Due to the additional formation of plate-like Al_2RE phase, El21+1% AlN/Al (T6) has a lower concentration of γ'' and β' precipitates than El21 (T6). Therefore, the creep rate of El21 (T6) decreases more significantly in the primary stage than that of El21+1% AlN/Al (T6).

II.   Duration of the secondary creep stage

Although El21 (T6) has a greater amount of γ'' and β' precipitates in the matrix to inhibit the dislocation movement in the primary creep stage, it reaches its tertiary creep stage rapidly after quite a narrow secondary creep stage. This is attributed to the overageing of precipitates and the thermal stability of the intermetallic particles.

The creep temperature in this work is 240 °C, which is higher than the ageing temperature of 200 °C. At such a relatively high temperature of 240 °C the nano-sized γ'' and β' precipitates

1 formed in El21 (T6) would become overaged and subsequently coarsen with the increasing

2 creep testing time after the primary creep stage. Argade *et al.* [70] investigated the

3 microstructures of hot-rolled Mg-4Y-3Nd alloys in peak-aged and overaged conditions using

4 TEM. They observed an obvious growth in precipitates with a length of more than 500 nm after

5 overageing. However, the precipitates in the peak-aged alloy show a length of approximately

6 200 nm. The coarsening of precipitates could change the dislocation-precipitate interaction

7 behavior. The retarding effects of precipitates against dislocation movement decrease as the

8 precipitates coarsen [71]. Therefore, the precipitate strengthening in El21 (T6) was weakened

9 and thus caused softening and a reduction of creep time to failure significantly.

10 Similarly, the precipitation strengthening from the γ'' and β' precipitates in El21+1% AlN/Al

11 (T6) was also weakened due to their dynamic overageing during creep testing at 240 °C.

12 However, the prominent intermetallic particles in El21+1% AlN/Al (T6) are quite different

13 from that in El21 (T6). The main second phase of El21+1% AlN/Al (T6) is Al_2RE particles

14 and the latter is $Mg_{41}RE_5$ (Table 2). The Al_2RE phase has a greater thermal stability than

15 $Mg_{41}RE_5$ [60]. This more thermally stable phase could help El21+1% AlN/Al (T6) endure

16 long-term elevated temperature creep testing. In addition, AlN NPs in El21+1% AlN/Al (T6)

17 have an excellent thermal stability with a significantly high melting point of 2800 °C [72],

18 indicating a superior thermal stability, which also contributes to longer durations of secondary

19 creep.

20 As aforementioned, the explanations for the longer secondary creep stage of El21+1% AlN/Al

21 (T6) and the narrow secondary creep stage of El21 (T6) also apply to the creep behaviors of

22 as-cast El21+1% AlN/Al and as-cast El21. Mg_3RE and Al_2RE are the two intermetallic phases

23 formed in as-cast El21+1% AlN/Al with the highest area fraction of 6.7 %. (Table 2). The

24 existence of the Al_2RE phase facilitates the thermal stability of as-cast El21+1% AlN/Al and

25 leads to its longer secondary creep period. In contrast, in the as-cast El21, Mg_3RE is the

26 dominant phase, which has a relatively lower melting point than the Al_2RE phase of 780 °C. It

27 has a lower thermal stability during creep and results in an earlier failure of the as-cast El21

28 alloy.

29 In summary, the minimum creep rates for all the investigated alloy/nanocomposite were largely

30 influenced by the pinning effects of dislocations via precipitates/intermetallic particles during

31 creep. Nevertheless, as creep deformation proceeded, the strengthening effects from nano-sized

32 precipitates were diminished due to their overaging. The thermal stability of intermetallic

25

particles then became the dominant factor in influencing the secondary creep stage and determining the creep properties.

5. Conclusions

The influence of T6 heat treatment on the microstructural evolution and creep performance of El21 and El21+1% AlN/Al nanocomposites were compared and discussed with respect to their as-cast states. The conclusions are as follows:

1) After T6 treatment, $Mg_{41}RE_5$ was the predominant intermetallic phase in El21 (T6) and many nano-sized γ'' and β' precipitates were observed. In El21+1% AlN/Al (T6), besides the particulate Al_2RE intermetallic phase, the additional plate-like Al_2RE precipitates were observed. Although the γ'' and β' precipitates formed in El21+1% AlN/Al (T6) were similar to that in El21 (T6), their concentration was estimated to be lower than that of the latter.

2) T6 treatment improved the creep resistance of El21. Although the area fraction of intermetallic particles decreased following T6 treatment, the precipitation strengthening resulting from the γ'' and β' precipitates in El21 (T6) overtook the reduction of creep resistance caused by the decreased grain boundary reinforcements, thus improving creep resistance. The creep resistance El21+1% AlN/Al nanocomposite deteriorated following T6 treatment. This was attributed to the decrease of precipitation strengthening and the decrease of grain boundary reinforcements in El21+1% AlN/Al (T6) nanocomposites.

3) El21 (T6) had a lower minimum creep rate with a shorter secondary creep stage than El21+1% AlN/Al (T6). El21 (T6) has a greater amount of precipitation strengthening during primary creep, which results in a lower minimum creep rate than El21+1% AlN/Al (T6). The shorter secondary creep stage of El21 (T6) is ascribed to precipitate overageing as a result of the longer creep testing time and the lower thermal stability of $Mg_{41}RE_5$ particles.

4) El21+1% AlN/Al nanocomposites, either in the as-cast or T6 conditions, always showed significantly longer durations of secondary creep stages than NP-free El21 alloy. This is primarily attributed to the addition of AlN NPs and the occurrence of particulate/plate Al_2RE in as-cast El21+1% AlN/Al and El21+1% AlN/Al (T6).

Declaration of Interest Statement

We declare that there is no known competing financial interests or personal relationships that could have appeared to influence the work reported in this paper.

Credit author statement

Hong Yang: Methodology, Investigation, Data curation, Roles/Writing - original draft, Writing-Review & Editing

Daniela Zander: Supervision, Resources, Writing-Review & Editing

Bin Jiang: Methodology, Resources, Writing-Review & Editing

Yuanding Huang: Methodology, Formal analysis, Writing-Review & Editing

Sarkis Gavras: Investigation, Formal analysis, Writing-Review & Editing

Karl Ulrich Kainer: Supervision, Resources, Writing-Review & Editing

Hajo Dieringa: Conceptualization, Formal analysis, Writing-Review & Editing

Acknowledgement

References

[1] M. Pekguleryuz, M. Celikin, Creep resistance in magnesium alloys, International Materials Reviews 55(4) (2010) 197-217.

[2] K.R. Athul, U.T.S. Pillai, A. Srinivasan, B.C. Pai, A review of different creep mechanisms in Mg alloys based on stress exponent and activation energy, Advanced Engineering Materials 18(5) (2016) 770-794.

[3] M. Celikin, Creep resistance in magnesium alloys International Materials Reviews 55(4) (2010) 197-217.

[4] A.A. Luo, B.R. Powell, M.P. Balogh, Creep and microstructure of magnesium-aluminum-calcium based alloys, Metallurgical and Materials Transactions A 33(3) (2002) 567-574.

[5] M.O. Pekguleryuz, E. Baril, Development of Creep Resistant Mg-Al-Sr Alloys, in: S.N. Mathaudhu, A.A. Luo, N.R. Neelameggham, E.A. Nyberg, W.H. Sillekens (Eds.), Essential Readings in Magnesium Technology, Springer International Publishing, Cham, 2016, pp. 283-289.

[6] H. Dieringa, Y. Huang, P. Wittke, M. Klein, F. Walther, M. Dikovits, C. Poletti, Compression-creep response of magnesium alloy DieMag422 containing barium compared with the commercial creep-resistant alloys AE42 and MRI230D, Materials Science and Engineering: A 585 (2013) 430-438.

[7] S. Gavras, S. Zhu, M.A. Easton, M.A. Gibson, H. Dieringa, Compressive creep behaviour of high-pressure die-cast aluminium-containing magnesium alloys developed for elevated temperature applications, Frontiers in Materials 6 (2019) 262.

[8] D. Amberger, P. Eisenlohr, M. Göken, Influence of microstructure on creep strength of MRI 230D Mg alloy, Journal of Physics: Conference Series 240 (2010) 012068.

[9] S.M. Zhu, M.A. Gibson, M.A. Easton, J.F. Nie, The relationship between microstructure and creep resistance in die-cast magnesium–rare earth alloys, Scripta Materialia 63(7) (2010) 698-703.

[10] B.L. Mordike, Creep-resistant magnesium alloys, Materials Science and Engineering: A 324(1) (2002) 103-112.

[11] M. Pekguleryuz, M. Celikin, Creep resistance in magnesium alloys, International Materials Reviews 55(4) (2013) 197-217.

[12] S. You, Y. Huang, K.U. Kainer, N. Hort, Recent research and developments on wrought magnesium alloys, Journal of Magnesium and Alloys 5(3) (2017) 239-253.

[13] S. Zhu, M.A. Easton, T.B. Abbott, J.-F. Nie, M.S. Dargusch, N. Hort, M.A. Gibson, Evaluation of magnesium die-casting alloys for elevated temperature applications: microstructure, tensile properties, and creep resistance, Metallurgical and Materials Transactions A 46(8) (2015) 3543-3554.

[14] M. Gibson, C. Bettles, M. Murray, G. Dunlop, S. Cashion, AM-HP2: A New Magnesium Alloy with Improved Diecastability and Creep Strength for Power‐train Applications, 13th Magnesium Automotive and End User Seminar, Aalen, 22nd-23rd September, 2005.

[15] P. Lyon, I. Syed, S. Heaney, Elektron 21 – An Aerospace Magnesium Alloy for Sand Cast and Investment Cast Applications, Advanced Engineering Materials 9(9) (2007) 793-798.

[16] L. Katsarou, M. Mounib, W. Lefebvre, S. Vorozhtsov, M. Pavese, C. Badini, J.M. Molina-Aldareguia, C.C. Jimenez, M.T. Pérez Prado, H. Dieringa, Microstructure, mechanical properties and creep of magnesium alloy Elektron21 reinforced with AlN nanoparticles by ultrasound-assisted stirring, Materials Science and Engineering: A 659 (2016) 84-92.

[17] R. Daudin, S. Terzi, C. Mallmann, R.S. Martín, P. Lhuissier, E. Boller, A. Pacureanu, L. Katsarou, H. Dieringa, L. Salvo, Indirect improvement of high temperature mechanical properties of a Mg-based alloy Elektron21 by addition of AlN nanoparticles, Materials Science and Engineering: A 688 (2017) 76-82.

[18] A. Saboori, E. Padovano, M. Pavese, H. Dieringa, C. Badini, Effect of solution treatment on precipitation behaviors, age hardening response and creep properties of Elektron21 alloy reinforced by AlN nanoparticles, Materials 10(12) (2017) 1380.

[19] H. Yang, Y. Huang, B. Song, K.U. Kainer, H. Dieringa, Enhancing the creep resistance of AlN/Al nanoparticles reinforced Mg-2.85Nd-0.92Gd-0.41Zr-0.29Zn alloy by a high shear dispersion technique, Materials Science and Engineering: A 755 (2019) 18-27.

[20] H. Yang, Y. Huang, S. Gavras, K.U. Kainer, N. Hort, H. Dieringa, Influences of AlN/Al Nanoparticles on the Creep Properties of Elektron21 Prepared by High Shear Dispersion Technology, Jom (2019).

[21] H. Yang, D. Zander, Y. Huang, K.U. Kainer, H. Dieringa, Individual/synergistic effects of Al and AlN on the microstructural evolution and creep resistance of Elektron21 alloy, Materials Science and Engineering: A (2020) 139072.

[22] H. Yang, Y. Huang, D. Tolnai, K.U. Kainer, H. Dieringa, Influences of Al and high shearing dispersion technique on the microstructure and creep resistance of Mg-2.85Nd-0.92Gd-0.41Zr-0.29Zn alloy, Materials Science and Engineering: A 764 (2019) 138215.

[23] J.-F. Nie, Precipitation and hardening in magnesium alloys, Metallurgical and Materials Transactions A 43(11) (2012) 3891-3939.

[24] L.L. Rokhlin, Magnesium alloys containing rare earth metals: structure and properties, Crc Press2003.

[25] B. Smola, I. Stulíková, J. Pelcová, B.L. Mordike, Significance of stable and metastable phases in high temperature creep resistant magnesium–rare earth base alloys, Journal of Alloys and Compounds 378(1) (2004) 196-201.

[26] A. Kiełbus, Microstructure and mechanical properties of Elektron 21 alloy after heat treatment, Journal of Achievements in Materials and Manufacturing Engineering 20(1-2) (2007) 127-130.

[27] A. Kielbus, T. Rzychon, Mechanical and creep properties of Mg-4Y-3RE and Mg-3Nd-1Gd magnesium alloy, Procedia Engineering 10 (2011) 1835-1840.

[28] M.I. Lerner, E.A. Glazkova, A.S. Lozhkomoev, N.V. Svarovskaya, O.V. Bakina, A.V. Pervikov, S.G. Psakhie, Synthesis of Al nanoparticles and Al/AlN composite nanoparticles by electrical explosion of aluminum wires in argon and nitrogen, Powder Technology 295 (2016) 307-314.

[29] H. Men, B. Jiang, Z. Fan, Mechanisms of grain refinement by intensive shearing of AZ91 alloy melt, Acta Materialia 58(19) (2010) 6526-6534.

[30] S. Tzamtzis, H. Zhang, N. Hari Babu, Z. Fan, Microstructural refinement of AZ91D die-cast alloy by intensive shearing, Materials Science and Engineering: A 527(12) (2010) 2929-2934.

[31] Z. Fan, Y. Wang, M. Xia, S. Arumuganathar, Enhanced heterogeneous nucleation in AZ91D alloy by intensive melt shearing, Acta Materialia 57(16) (2009) 4891-4901.

[32] Z. Fan, G. Liu, Solidification behaviour of AZ91D alloy under intensive forced convection in the RDC process, Acta Materialia 53(16) (2005) 4345-4357.

[33] L.M.T. Elektron21, Data sheet 455.

[34] I. Pikos, T. Rzychoń, A. Kiełbus, Microstructural phenomenon occurring in Elektron 21 magnesium alloy during Creep, Materials Science Forum, Trans Tech Publ, 2014, pp. 339-343.

[35] A.A. Luo, Recent magnesium alloy development for elevated temperature applications, International Materials Reviews 49 (2004) 13-30.

[36] A. ASTM, E 3-11: Standard guide for preparation of metallographic specimens, ASTM International (2011).

[37] V. Kree, J. Bohlen, D. Letzig, K. Kainer, The metallographical examination of magnesium alloys, Praktische Metallographie-Practical Metallography 41(5) (2004) 233-246.

[38] A. Standard, E112-13, Standard test method for determining average grain size. West Conshohocken, PA (2013) 1-28.

[39] J. Schindelin, I. Arganda-Carreras, E. Frise, V. Kaynig, M. Longair, T. Pietzsch, S. Preibisch, C. Rueden, S. Saalfeld, B. Schmid, Fiji: an open-source platform for biological-image analysis, Nature methods 9(7) (2012) 676-682.

[40] K.-L. Lin, Phase identification using series of selected area diffraction patterns and energy dispersive spectrometry within TEM, Microscopy Research 2(04) (2014) 57.

[41] B. Fultz, J.M. Howe, Transmission electron microscopy and diffractometry of materials, Springer Science & Business Media2012.

[42] D.B. Williams, C.B. Carter, Diffraction in TEM, Transmission Electron Microscopy, Springer2009, pp. 197-209.

[43] S.L. Chen, F. Zhang, F.Y. Xie, S. Daniel, X.Y. Yan, Y.A. Chang, R. Schmid-Fetzer, W.A. Oates, Calculating phase diagrams using PANDAT and panengine, JOM 55(12) (2003) 48-51.

[44] Q. Chen, A. Tang, J. Ye, L. Hao, Y. Wang, T. Zhang, Equilibrium and metastable phases in a designed precipitation hardenable Mg–3Gd–3Nd–0.6Zr alloy, Materials Science and Engineering: A 686 (2017) 26-33.

[45] P. Villars, Pearson's handbook of crystallographic data for intermetallic phases, Desk Edition, American Society for Metals, Metal Park, OH 170 (1997).

[46] J. Zhang, J. Wang, X. Qiu, D. Zhang, Z. Tian, X. Niu, D. Tang, J. Meng, Effect of Nd on the microstructure, mechanical properties and corrosion behavior of die-cast Mg–4Al-based alloy, Journal of Alloys and Compounds 464(1) (2008) 556-564.

[47] A. Kielbus, T. Rzychon, R. Przeliorz, DSC and microstructural investigations of the Elektron 21 magnesium alloy, Materials Science Forum 638-642 (2010) 1447-1452.

[48] L. Ma, R.K. Mishra, M.P. Balogh, L. Peng, A.A. Luo, A.K. Sachdev, W. Ding, Effect of Zn on the microstructure evolution of extruded Mg–3Nd (–Zn)–Zr (wt.%) alloys, Materials Science and Engineering: A 543 (2012) 12-21.

[49] P.A. Nuttall, T.J. Pike, B. Noble, Metallography of dilute Mg-Nd-Zn alloys, Metallography 13(1) (1980) 3-20.

[50] Y. Li, T.G. Langdon, A unified interpretation of threshold stresses in the creep and high strain rate superplacticity of metal matrix composites, Acta Metallurgica 47 (1999) 3395-3403.

[51] Y. Li, T.G. Langdon, A simple procedure for estimating threshold stresses in the creep of metal matrix conposites, Scripta Materialia 36 (1997) 1457-1460.

[52] N. Mo, Q. Tan, M. Bermingham, Y. Huang, H. Dieringa, N. Hort, M.-X. Zhang, Current development of creep-resistant magnesium cast alloys: A review, Materials & Design 155 (2018) 422-442.

[53] M.A. Easton, M.A. Gibson, D. Qiu, S.M. Zhu, J. Gröbner, R. Schmid-Fetzer, J.F. Nie, M.X. Zhang, The role of crystallography and thermodynamics on phase selection in binary magnesium–rare earth (Ce or Nd) alloys, Acta Materialia 60(11) (2012) 4420-4430.

[54] M.-X. Zhang, P. Kelly, Edge-to-edge matching model for predicting orientation relationships and habit planes—The improvements, Scripta Materialia 52(10) (2005) 963-968.

[55] M.-X. Zhang, P. Kelly, M. Easton, J. Taylor, Crystallographic study of grain refinement in aluminum alloys using the edge-to-edge matching model, Acta Materialia 53(5) (2005) 1427-1438.

[56] M.-X. Zhang, P. Kelly, Understanding the crystallography of the eutectoid microstructure in a Zn–Al alloy using the edge-to-edge matching model, Scripta materialia 55(7) (2006) 577-580.

[57] S. Delfino, A. Saccone, R. Ferro, Phase relationships in the neodymium-magnesium alloy system, Metallurgical Transactions A 21(8) (1990) 2109-2114.

[58] K. Saito, K. Hiraga, The structures of precipitates in an Mg-0.5 at% Nd age-hardened alloy studied by HAADF-STEM technique, Materials Transactions (2011) 1109051461-1109051461.

[59] D.H. Ping, K. Hono, J.F. Nie, Atom probe characterization of plate-like precipitates in a Mg–RE–Zn–Zr casting alloy, Scripta Materialia 48(8) (2003) 1017-1022.

[60] N. Hort, Y. Huang, K.U. Kainer, Intermetallics in magnesium alloys, Advanced Engineering Materials 8(4) (2006) 235-240.

[61] J. Zhang, S. Liu, Z. Leng, X. Liu, Z. Niu, M. Zhang, R. Wu, Structure stability and mechanical properties of high-pressure die-cast Mg–Al–La–Y-based alloy, Materials Science and Engineering: A 531 (2012) 70-75.

[62] A. Koltsov, F. Hodaj, N. Eustathopoulos, A. Dezellus, P. Plaindoux, Wetting and interfacial reactivity in Ag–Zr/sintered AlN system, Scripta Materialia 48(4) (2003) 351-357.

[63] J. Murray, Phase diagrams of binary magnesium alloys, Ohio, ASM International (1988) 17-34.

[64] X. zheng, L. Wang, J. wang, Y. Wu, Z. Ning, J. Sun, L. Wang, Microstructure and mechanical properties of Mg–4Al–4Nd–0.5Zn–0.3Mn alloy, Materials Science and Engineering: A 515(1) (2009) 98-101.

[65] M. Li, H. Hao, A. Zhang, Y. Song, X. Zhang, Effects of Nd on microstructure and mechanical properties of as-cast Mg-8Li-3Al alloy, Journal of Rare Earths 30(5) (2012) 492-496.

[66] M.S. Dargusch, S.M. Zhu, J.F. Nie, G.L. Dunlop, Microstructural analysis of the improved creep resistance of a die-cast magnesium–aluminium–rare earth alloy by strontium additions, Scripta Materialia 60(2) (2009) 116-119.

[67] S. Zhu, M.A. Easton, T.B. Abbott, M.A. Gibson, J.-F. Nie, The influence of individual rare earth elements (La, Ce, or Nd) on creep resistance of die-cast magnesium alloy AE44 Advanced Engineering Materials 18(6) (2016) 932-937.

[68] J.F. Nie, Effects of precipitate shape and orientation on dispersion strengthening in magnesium alloys, Scripta Materialia 48(8) (2003) 1009-1015.

[69] F. Abe, Development of creep-resistant steels and alloys for use in power plants, Structural Alloys for Power Plants, Elsevier2014, pp. 250-293.

[70] G.R. Argade, S.K. Panigrahi, R.S. Mishra, Aging response on the stress corrosion cracking behavior of wrought precipitation-hardened magnesium alloy, Journal of Materials Science 55(3) (2020) 1216-1230.

[71] P. Sepehrband, X. Wang, H. Jin, S. Esmaeili, Interactive microstructural phenomena during non-isothermal annealing of an Al-Mg-Si-Cu alloy, Materials Characterization 137 (2018) 212-221.

[72] G.A. Slack, T.F. McNelly, Growth of high purity AlN crystals, Journal of Crystal Growth 34(2) (1976) 263-279.